# Discharges generated at metal-semiconductor-gas triple junctions in air at atmospheric pressure

David Z. Pai, David Babonneau, Sophie Camelio

*Institut PPRIME (CNRS UPR 3346, Université de Poitiers, ISAE-ENSMA)*
*Bd Marie & Pierre Curie BP 30179, 86962 Futuroscope, France*

**Abstract:** Atmospheric-pressure plasmas are generated at tungsten/silicon/air triple junctions. Current-voltage measurements, optical emission spectroscopy, and Raman spectroscopy are employed to characterize the plasma and surface. The discharge is found to have properties distinct from other nanosecond or dielectric barrier discharges, in terms of the range of generated current and the role of the silicon 'barrier'.

**Keywords:** nanosecond discharge, microplasma, plasma-semiconductor interface

## 1. Introduction

The use of semiconductors in atmospheric-pressure plasma science has led to the development of microplasma-based electronic and optical devices [1, 2]. By taking advantage of well-developed microfabrication techniques, it is possible to machine tightly packed arrays of microplasmas with high precision, leading to the development of new light sources [3, 4]. Conversely, the involvement of atmospheric-pressure plasmas in conventional semiconductor device technology has largely been in the role of an undesired effect, namely that of surface flashover [5-8]. In this case, high-voltage semiconductor switches suffered from the problem that a discharge would be generated along the surface of the semiconductor at average applied electric fields lower than the breakdown threshold of the semiconductor.

An explanation of the flashover phenomenon in silicon is discussed in [6], based upon experiments whereby pulsed high voltage is applied across silicon in vacuum conditions. Upon application of the voltage pulse, ohmic and injection currents are generated initially within the silicon. As the applied electric field increases, avalanche current in the silicon increases near defects and concentrates near the surface. This surface current causes heating and desorption from the silicon into vacuum, thus providing a gaseous medium for ionization. With the addition of seed electrons originating at the metal-semiconductor-vacuum triple junction, a gas discharge can be generated leading to surface flashover. The above model of surface flashover was considered primarily from the semiconductor physics point of view, with only a very general description of the gas discharge.

In this work, we wish to reconsider the problem of plasma generation along semiconductor surfaces. While drawing from previous work on surface flashover, we will focus instead on the metal-semiconductor-gas triple junction. The reactor geometry will resemble that of a surface dielectric barrier discharge (DBD) rather than the direct gap geometry studied in previous work on surface flashover. Also, we will be working in atmospheric-pressure conditions rather than vacuum.

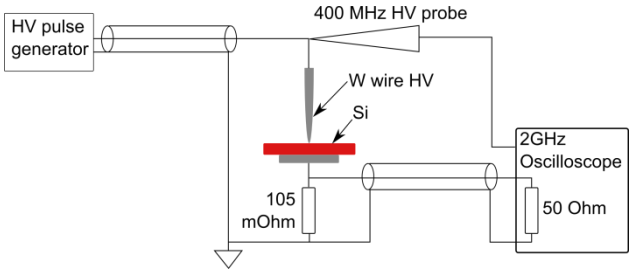


Figure 1. Schematic diagram of the discharge circuit.

## 2. Experimental Setup

The plasma is generated in ambient atmospheric-pressure air in a surface DBD geometry, as shown in Figure 1. The anode is a tungsten wire (Goodfellow 99.95% purity) with a diameter of 40 µm placed in mechanical contact with the polished side of silicon (n-type, 1 – 10 Ω-cm, 280-µm thickness). Proper electrical contact at the triple junction is checked by adjusting the position of the wire during discharge generation. No change in the current upon moving the wire towards the silicon indicates that there is no gap between wire and the silicon. A copper contact is adhered to the unpolished side of the silicon using high-conductivity silver epoxy paste (Polytec EC 101).

High voltage is applied to the anode using a generator producing nanosecond-duration pulses (FID Technology FPG 40-30 NK), with a fixed pulse repetition frequency of 100 Hz. The applied voltage is measured using a passive probe (Lecroy PPE 6 kV) with 400 MHz bandwidth. A 105-mΩ current-sensing resistor is inserted in series with the plasma circuit on the ground side, between the copper contact and the ground plane. The voltage generated across the sensing resistor is measured using a 50-Ω coaxial cable that terminates into a 50-Ω input impedance on the oscilloscope channel. The current and voltage signals are acquired using an oscilloscope (Lecroy Waverunner 204 MXI) with 2-GHz bandwidth.

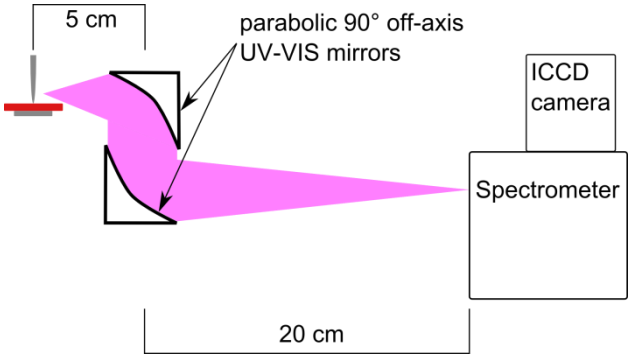


Figure 2. Schematic diagram of the setup for OES and fast imaging.

Optical diagnostics are also employed to characterize the discharge. UV-VIS optical emission spectroscopy (OES) and fast imaging are performed using the setup shown in Figure 2. Light from the discharge is collected and focused on the entrance slit of a spectrograph (Acton SP2500i) using two UV-VIS parabolic 90° off-axis mirrors (Edmund Optics) with focal lengths of 5 and 20 cm, respectively, to provide a magnification of 4X. The diffracted light is detected using an intensified CCD (ICCD) camera (Princeton Instruments PIMAX 1).

Raman microspectroscopy and microscopic imaging are performed using the setup shown in Figure 3. An argon ion laser (Spectra Physics Stabilite 2017) produces a CW beam at 488 nm that is focused onto the silicon surface via a 50X microscope objective (Mitutoyo M Plan Apo). The output power of the laser is set to 40 mW, but the laser power reaching the focal point is adjusted from 0.02 to 20 mW using neutral density filters. The backscattered light is filtered first through a dichroic mirror (Semrock RazorEdge), focused through a lens with a focal length of 20 cm, and then filtered again through a notch filter (Semrock StopLine). The Raman signal is focused onto the entrance slit of a spectrometer (Ocean Optics HR2000+) with an instrumental function of 6 $cm^{-1}$. For imaging, the silicon surface can be illuminated using a tungsten lamp. Images are recorded using a CMOS camera (Thorlabs DCC1545C).

## 3. Results and discussion

First, we consider the breakdown threshold. At an applied voltage amplitude of $V_p$ = 650 V, there is no detectable current pulse due to a discharge, as shown in Figure 4 (black). The current up to $t$ = 2 ns can be shown to be consistent with a displacement current due to a 0.6 pF capacitance. Unstable breakdown occurs at $V_p$ = 800 V, with shot-to-shot variation of the current. Two phases in the current waveform can be identified. The first is about 100 mA in amplitude and can appear alone starting at $t$ = 10 ns, as shown in Figure 4 (red). Here, the silicon remains capacitive in nature, because the current pulse is similar in amplitude and duration to those characteristic of surface DBDs generated in similar conditions but with an alumina dielectric barrier [9].

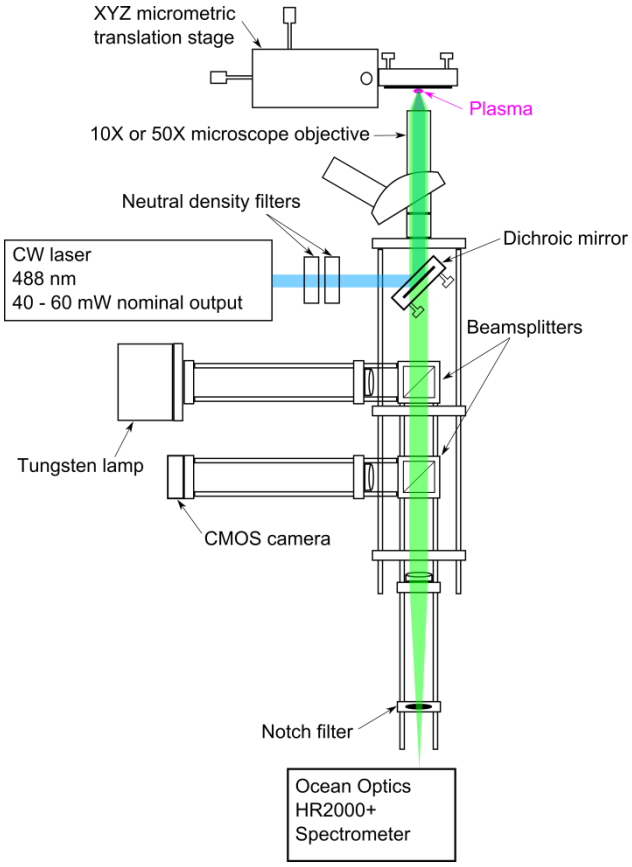


Figure 3. Schematic diagram of the setup for Raman microspectroscopy.

Occurring more frequently is the case where this first phase is followed by a second phase starting at $t_{on}$ = $t$ = 18 ns that reaches several hundred mA in amplitude, as shown in Figure 4 (green). The second phase begins 4 ns after when the applied voltage has reached its maximum value. The plasma thus acts as the ohmic contact that enables the silicon to switch into a highly conducting state. The tungsten-silicon contact does not provide this switch, and this is critical for allowing plasma generation. When the anode contact with the silicon is made using silver epoxy, the silicon enters a conducting state even at low voltage. The resistance of the silicon is too low for the applied voltage to increase up to the breakdown threshold. With a mechanical contact, the applied voltage can be increased sufficiently high to generate plasma.

The current amplitude $I_p$ can be varied continuously from the 'low-current' case where $I_p$ < 1 A (Figure 4) up to 20 A (Figure 5) by varying $V_p$ from 800 to 1600 V. For nanosecond repetitively pulsed (NRP) microplasmas generated in a metal pin-to-pin electrode configuration, with similar discharge length and $V_p$ as in this study, the attainable values of $I_p$ are typically in the 7 – 12 A range [10]. NRP glow and spark discharges of mm length also cover narrower ranges of $I_p$ [11, 12]. Thus, the triple junction discharge has the widest current range of any nanosecond discharge regime.

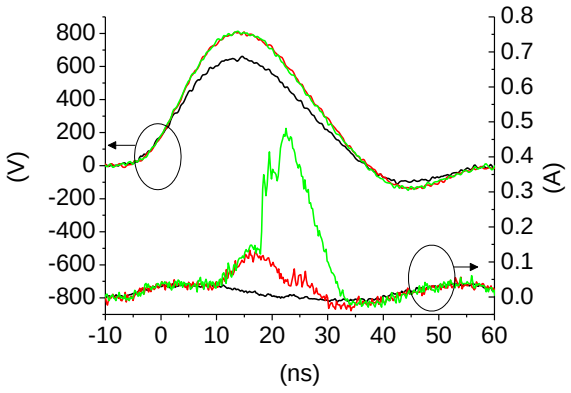


Figure 4. Measured applied voltage and total current below (black) and at the breakdown threshold (red, green), i.e. the 'low-current' case.

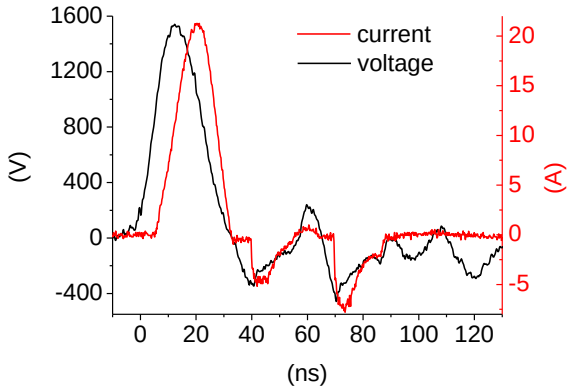


Figure 5. Measured applied voltage and current above the breakdown threshold, i.e. the 'high-current' case.

The current waveform can be characterized in terms of its rise and fall times. For the second phase of the low-current case shown in Figure 4, the 10%-90% rise and fall times of the current pulse are $\tau_{rise}$ = 3.4 ns and $\tau_{fall}$ = 7.7 ns, respectively. For the first current pulse of the high-current case, $\tau_{rise}$ = 10.4 ns and $\tau_{fall}$ = 8 ns. The difference in $\tau_{rise}$ is even more marked for negative current pulses, with $\tau_{rise}$ = 1.2 ns and $\tau_{fall}$ = 8.2 ns for the pulse occurring at $t$ = 40 ns in Figure 5. Though the rise time is variable, the fall time remains similar in all cases.

Typical images of the discharge for the 'high-current' case are shown in Figure 6. The CMOS camera image integrated over 1 s, collecting light from 100 consecutive high-voltage pulses, shows that the discharge extends beyond the metal-semiconductor-gas junction by about 100 µm. Single-shot ICCD imaging integrated over 1 ms confirms that this is representative of each pulse. Unlike the extended high-current case, the discharge remains contained in the junction for the low-current case. The difference in discharge size may also account for the difference in current amplitude and rise time between the two cases.

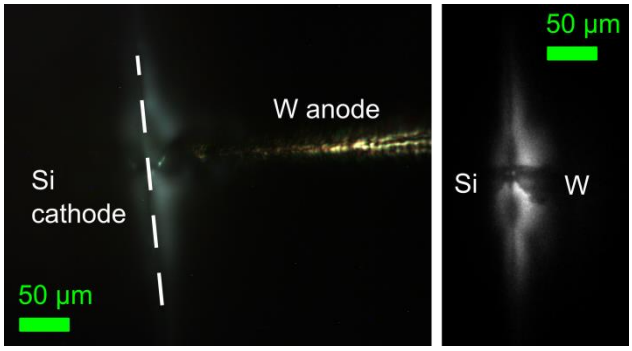


Figure 6. Side-view images of the 'high-current' case with 1-s (left) and 1-ms single shot (right) exposure times.

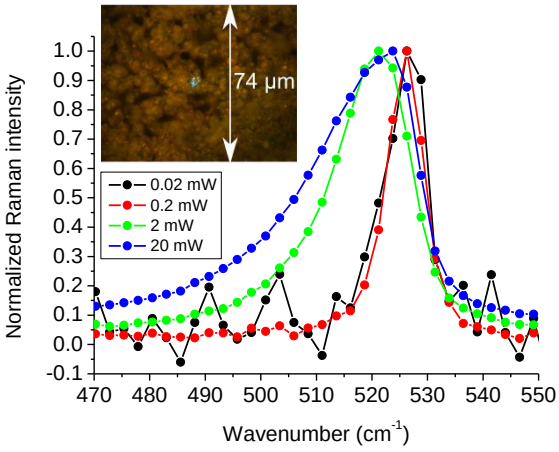


Figure 7. Raman spectra of the silicon surface after operating the discharge in the 'high-current' case, for different levels of nominal laser power.

Although not shown here, time-integrated optical emission spectra of the plasma show many similarities with those of NRP microplasmas generated in nearly identical conditions except that the plasma is generated between two tungsten electrodes separated by 200 µm [10] rather than at a triple junction. This may indicate that the electric field at the triple junction is similar to that of NRP microplasmas, whose spatially averaged values can reach over 600 Td [13]. The distinguishing feature of the plasma chemistry, as in the case of NRP microplasmas [14], is that there is a strong presence of N and $N^+$ in the spectra that is typically not observed in the bulk of mm-scale plasmas generated in similar conditions [15].

Ex-situ Raman spectroscopy has been performed to assess the effect of the plasma on the silicon surface. Two main observations can so far be made. First, besides the crystalline Si peak near 520 $cm^{-1}$, there can also be two peaks near 709 and 810 $cm^{-1}$ that can be assigned to the W=O stretching and bending modes of $WO_3$, respectively. The Raman peaks of $WO_3$ are only ever found within a ~30 µm radius of the triple junction, indicating localized deposition of sputtered electrode

material that does not extend the full length of the discharge.

Second, laser power has a strong effect on the Si peak, as shown in Figure 7. At low nominal laser power of 0.02 or 0.2 mW, the Si peak is centered at about 527 $cm^{-1}$ and has a FWHM of about 20 $cm^{-1}$, which is similar in profile to untreated Si. At high nominal laser power of 2 or 20 mW, the peak undergoes significant broadening and shift to lower wavenumber. Such changes to the Raman spectrum of Si with laser power have been observed previously in microcrystalline [16] and nanocrystalline [17] Si and are attributed to high temperatures reached when the localized heat dissipation is much poorer than for bulk silicon. The image of the surface shown in the inset of Figure 7 indeed shows a microstructured morphology.

## 4. Conclusion

Nanosecond discharges at tungsten/silicon/atmospheric-pressure air triple junctions have been characterized using current-voltage measurements, optical emission spectroscopy, and ex-situ Raman spectroscopy. Unlike dielectric barriers in a similar surface DBD geometry, silicon is an active barrier that appears to switch from an insulating to conducting state during plasma generation. This enables the triple junction discharge to achieve a wider range of currents than possible with other nanosecond discharges. The discharge can propagate along the surface, away from the triple junction, and may cause structuration at the micro- or nano-scale. The silicon barrier thus allows for high currents that are not obtainable with a dielectric barrier. On the other hand, the silicon is not simply a ballast resistor either, because some degree of discharge propagation is possible, like with a DBD. The discharges generated can also be very small (<10 µm) when confined to the triple junction, and may thus be a convenient way of generating very small microplasmas that are possibly in the field emission regime of operation [18]. This would be consistent with the high electric field anticipated as necessary for the observed production of atomic neutral and ion species in this study.

## 5. Acknowledgements

This work has been supported by the Agence Nationale de la Recherche program PLASMAFACE (ANR-15-CE06-0007-01), the French Government program “Investissements d’Avenir” (LABEX INTERACTIFS, ANR-11-LABX-0017-01), the Poitou-Charentes region (CPER program), and the European Union (FEDER/FSE/FEADER programs).

## 6. References

[1] K.-F. Chen and J. Eden, Appl. Phys. Lett. **93**, 161501 (2008).
[2] N. Ostrom and J. Eden, Appl. Phys. Lett. **87**, 141101 (2005).
[3] L. Schwaederlé, M. Kulsreshath, L. Overzet, P. Lefaucheux, T. Tillocher, and R. Dussart, Journal of Physics D: Applied Physics **45**, 065201 (2012).
[4] S.-J. Park, K.-F. Chen, N. Ostrom, and J. Eden, Appl. Phys. Lett. **86**, 111501 (2005).
[5] F. E. Peterkin, T. Ridolfi, L. L. Buresh, B. J. Hankla, D. Scott, P. Williams, W. C. Nunnally, and B. Thomas, IEEE Transactions on Electron Devices **37**, 2459 (1990).
[6] G. Gradinaru and T. Sudarshan, J. Appl. Phys. **73**, 7643 (1993).
[7] W.-B. Zhao, G.-J. Zhang, M. Dong, and Z. Yan, Journal of Physics D: Applied Physics **40**, 7419 (2007).
[8] J. Gleizer, Y. E. Krasik, and J. Leopold, J. Appl. Phys. **117**, 073301 (2015).
[9] R. Brandenburg, H. Grosch, T. Hoder, and K. D. Weltmann, European Physical Journal-Applied Physics **55**, 13813 (2011).
[10] T. Orriere, E. Moreau, N. Benard, and D. Z. Pai, *68th Gaseous Electronics Conference*, Honolulu, October 12-16, 2015.
[11] D. Z. Pai, D. A. Lacoste, and C. O. Laux, Plasma Sources Sci. Technol. **19**, 065015 (2010).
[12] D. Z. Pai, G. D. Stancu, D. A. Lacoste, and C. O. Laux, Plasma Sources Sci. Technol. **18**, 045030 (2009).
[13] T. Orriere, E. Moreau, N. Benard, and D. Z. Pai, *23rd International Symposium on Plasma Chemistry*, Montreal, July 30-August 4, 2017.
[14] T. Orriere, E. Moreau, N. Benard, and D. Z. Pai, *HAKONE XV*, Brno, September 11-16, 2016.
[15] D. L. Rusterholtz, PhD, Ecole Centrale Paris, 2012.
[16] M. R. Abel, T. L. Wright, W. P. King, and S. Graham, IEEE Transactions on components and packaging technologies **30**, 200 (2007).
[17] S. Piscanec, M. Cantoro, A. Ferrari, J. Zapien, Y. Lifshitz, S. Lee, S. Hofmann, and J. Robertson, Phys. Rev. B **68**, 241312 (2003).
[18] P. Rumbach and D. B. Go, J. Appl. Phys. **112**, 103302 (2012).